

Towards Robust Hyperspectral Anomaly Detection: Decomposing Background, Anomaly, and Mixed Noise via Convex Optimization

Koyo Sato, *Student Member, IEEE*, and Shunsuke Ono, *Senior Member, IEEE*

Abstract—We propose a novel hyperspectral (HS) anomaly detection method that is robust to various types of noise. Most of existing HS anomaly detection methods are designed for cases where a given HS image is noise-free or is contaminated only by small Gaussian noise. However, in real-world situations, observed HS images are often degraded by various types of noise, such as sparse noise and stripe noise, due to sensor failure or calibration errors, significantly affecting the detection performance. To address this problem, this article establishes a robust HS anomaly detection method with a mechanism that can properly remove mixed noise while separating background and anomaly parts. Specifically, we newly formulate a constrained convex optimization problem to decompose background and anomaly parts, and three types of noise from a given HS image. Then, we develop an efficient algorithm based on a preconditioned variant of a primal-dual splitting method to solve this problem. Through comparison with existing methods, including state-of-the-art ones, we illustrate that the proposed method achieves a detection accuracy comparable to state-of-the-art methods in noise-free cases and is significantly more robust than these methods in noisy cases.

Index Terms—Hyperspectral anomaly detection, convex optimization

I. INTRODUCTION

HYPERSPECTRAL (HS) images are three-dimensional data with two-dimensional spatial and one-dimensional spectral information. HS images have hundreds of rich spectral bands, including both visible and invisible bands, allowing us to identify the detailed information of the imaged targets. Therefore, many HS image analysis technologies, including classification, unmixing, and anomaly detection, have been studied [1]–[5].

HS anomaly detection is the task of identifying an anomaly part, i.e., a set of pixels whose spectral signatures differ significantly from surrounding pixels, while suppressing a background part without prior information. It is important as a first step in HS image analysis because it can identify regions of interest that may contain potential targets and has applications in military defense, search and rescue operations, mine detection, and environmental monitoring [3]–[7]. Existing HS anomaly detection methods are roughly classified into four

groups: statistics-based methods, e.g., [8]–[13], reconstruction-based methods, e.g., [14]–[17], decomposition-based methods, e.g., [18]–[24], and deep learning-based methods, e.g., [25]–[28].

Statistics-based methods are designed to represent a background part with a certain probability distribution. These methods are the most classical approaches, and many methods have been proposed [8]–[13]. However, their detection performance is limited due to the difficulty of representing the complex structure of HS images with a single probability distribution.

Reconstruction-based methods are designed based on the assumption that background pixels can be represented by a certain dictionary, but anomaly pixels cannot. In general, for each test pixel, the surrounding pixels are used as a dictionary. Typical examples are sparse-representation (SR)-based methods, e.g., [14], [15], and collaborative-representation (CR)-based methods, e.g., [16], [17], where the SR-based methods reconstruct each test pixel with some elements of the dictionary, while the CR-based methods reconstruct it with all the elements.

In decomposition-based methods, a background part and an anomaly part are modeled by functions that capture their nature. Each part is estimated by solving an optimization problem involving these functions. Representative examples are low-rank representation (LRR)-based methods, e.g., [18]–[24], which decompose an HS image by exploiting the fact that the background part is low-rank and the anomaly part is sparse.

Among deep learning-based methods, autoencoder (AE)-based methods, e.g., [25]–[28], have received considerable attention in HS anomaly detection. The basic strategy of these methods is to train the network to reconstruct only a background part from a given HS image.

Most existing HS anomaly detection methods, including the ones reviewed above, are based on the assumption that an HS image consists only of a background part and an anomaly part. However, HS images are superimposed with various types of noise, such as Gaussian, sparse, and stripe noise, due to sensor failure, scanning methods, calibration errors, and other reasons [29]. In such images, it is difficult to distinguish between noise and anomalies, which significantly degrades the detection performance of the existing methods. Some existing methods take into account the effects of noise, such as [20], [22], [28], but most of them only deal with a small amount of Gaussian noise and are not robust to the above-mentioned mixed noise.

K. Sato is with the Department of Computer Science, Tokyo Institute of Technology, Yokohama, 226-8503, Japan (e-mail: sato.k.cf@m.titech.ac.jp).

S. Ono is with the Department of Computer Science, Tokyo Institute of Technology, Yokohama, 226-8503, Japan (e-mail: ono@c.titech.ac.jp).

This work was supported in part by JST PRESTO under Grant JPMJPR21C4 and JST AdCORP under Grant JPMJKB2307, and in part by JSPS KAKENHI under Grant 22H03610, 22H00512, and 23H01415.

One way to deal with such mixed noise is to apply an appropriate denoising method prior to anomaly detection. However, this approach is problematic from the point of view of validity and reliability, as over-smoothing during noise removal may result in missing information important for HS anomaly detection. There is also the problem of increased computational time due to the two-step processing. Therefore, a very important research direction is to develop an HS anomaly detection technique that can simultaneously perform the removal of various types of noise and the extraction of an anomaly part, and be robust enough in real-world applications.

Based on the above discussion, in this article, we propose a novel decomposition-based HS anomaly detection method that can accurately extract an anomaly part from a given HS image containing various types of noise. The main contributions of this article are as follows:

- (*Being robust to mixed noise*): To explicitly handle mixed noise, we consider a novel observation model in which an HS image is the sum of background and anomaly parts, and Gaussian, sparse, and stripe noise. We formulate a constrained convex optimization problem with functions and constraints that properly characterize each part and the three types of noise, allowing for robust decomposition.
- (*Reduction of interdependent hyperparameters*): In the proposed formulation, instead of adding terms characterizing the various types of noise to the objective function, they are imposed as hard constraints. This transforms complex interdependent hyperparameters into independent parameters that can be easily set. The advantages of such constrained formulations have been addressed in the literature of signal recovery, e.g., in [30]–[34].
- (*Automatic stepsize selection in optimization*): To solve the constrained convex optimization problem, we develop an efficient algorithm based on a Preconditioned variant of a Primal-Dual Splitting method (P-PDS) [35] with Operator-norm-based design method of Variable-wise Diagonal Preconditioning (OVDP) [36], [37]. This method can automatically determine the appropriate stepsize, i.e., our method is free from troublesome stepsize adjustment.

The remainder of this article is organized as follows. In Sec. II, we introduce several mathematical tools required for the proposed method. Sec. III presents the problem formulation and optimization algorithm of the proposed method. In Sec. IV, we demonstrate the superiority of the proposed method over existing methods including state-of-the-art ones through comprehensive experiments. Finally, Sec. V concludes this article.

The preliminary version of this work, without mathematical details, the generalization of a background part modeling, more extensive experiments, or deeper discussion, has appeared in conference proceedings [38].

II. PRELIMINARIES

In this section, we introduce minimal mathematical tools required for the proposed method. Readers interested in more details are referred to [39], [40]. The notations and definitions we used in this article are given in Table I.

TABLE I
NOTATIONS AND DEFINITIONS.

Notations	Definitions
\mathbb{R}	set of real numbers
x	scalar, $x \in \mathbb{R}$
\mathbf{x}	vector, $\mathbf{x} \in \mathbb{R}^{d_1}$
x_i	i -th element of a vector \mathbf{x}
$\ \mathbf{x}\ _2$	ℓ_2 -norm of a vector \mathbf{x} , $\ \mathbf{x}\ _2 := \sqrt{\sum_i x_i^2}$
\mathbf{X}	matrix, $\mathbf{X} \in \mathbb{R}^{d_1 \times d_2}$
\mathcal{X}	tensor, $\mathcal{X} \in \mathbb{R}^{d_1 \times d_2 \times d_3}$
$x_{i,j,k}, [\mathcal{X}]_{i,j,k}$	(i, j, k) -th element of a tensor \mathcal{X}
$[\mathcal{X}]_{i,j,:}$	(i, j) -th tube of a tensor \mathcal{X} , $[\mathcal{X}]_{i,j,:} \in \mathbb{R}^{d_3}$
\mathcal{O}	zero tensor
$\ \mathcal{X}\ _1$	ℓ_1 -norm of a tensor \mathcal{X} , $\ \mathcal{X}\ _1 := \sum_{i,j,k} x_{i,j,k} $
$\ \mathcal{X}\ _F$	Frobenius norm of a tensor \mathcal{X} , $\ \mathcal{X}\ _F := \sqrt{\sum_{i,j,k} x_{i,j,k}^2}$
$\ \mathcal{X}\ _{2,1}$	$\ell_{2,1}$ -norm of a tensor \mathcal{X} , $\ \mathcal{X}\ _{2,1} := \sum_{i,j} \sqrt{\sum_k x_{i,j,k}^2}$
\mathfrak{D}_v	vertical difference operator, $[\mathfrak{D}_v(\mathcal{X})]_{i,j,k} := \begin{cases} x_{(i+1),j,k} - x_{i,j,k}, & (1 \leq i < d_1) \\ 0, & (i = d_1) \end{cases}$
\mathfrak{D}_h	horizontal difference operator, $[\mathfrak{D}_h(\mathcal{X})]_{i,j,k} := \begin{cases} x_{i,(j+1),k} - x_{i,j,k}, & (1 \leq j < d_2) \\ 0, & (j = d_2) \end{cases}$
\mathfrak{D}_b	spectral difference operator, $[\mathfrak{D}_b(\mathcal{X})]_{i,j,k} := \begin{cases} x_{i,j,(k+1)} - x_{i,j,k}, & (1 \leq k < d_3) \\ 0, & (k = d_3) \end{cases}$
\mathcal{L}^*	adjoint operator of a linear operator \mathcal{L}
$\mathcal{L}_1 \circ \mathcal{L}_2$	composition of linear operators \mathcal{L}_1 and \mathcal{L}_2
$\ \mathcal{L}\ _{\text{op}}$	operator norm of a linear operator, $\ \mathcal{L}\ _{\text{op}} := \sup_{\mathcal{X} \neq \mathcal{O}} \frac{\ \mathcal{L}(\mathcal{X})\ _F}{\ \mathcal{X}\ _F}$
$\mathcal{B}_{F,\varepsilon}^{\mathcal{Y}}$	Frobenius norm ball with center \mathcal{Y} and radius ε , $\mathcal{B}_{F,\varepsilon}^{\mathcal{Y}} := \{\mathcal{X} \in \mathbb{R}^{d_1 \times d_2 \times d_3} \mid \ \mathcal{X} - \mathcal{Y}\ _F \leq \varepsilon\}$
$\mathcal{B}_{1,\alpha}$	ℓ_1 -norm ball with center \mathcal{O} and radius α , $\mathcal{B}_{1,\alpha} := \{\mathcal{X} \in \mathbb{R}^{d_1 \times d_2 \times d_3} \mid \ \mathcal{X}\ _1 \leq \alpha\}$

A. Proximal Tools

Let $\mathcal{X} \in \mathbb{R}^{D(=d_1 \times d_2 \times d_3)}$, and $\Gamma_0(\mathbb{R}^D)$ be the set of all proper lower-semicontinuous convex functions¹ on \mathbb{R}^D . For any $\gamma > 0$, the proximity operator of a function $f \in \Gamma_0(\mathbb{R}^D)$ is defined by

$$\text{prox}_{\gamma f}(\mathcal{X}) := \underset{\mathcal{Y} \in \mathbb{R}^D}{\text{argmin}} f(\mathcal{Y}) + \frac{1}{2\gamma} \|\mathcal{X} - \mathcal{Y}\|_F^2. \quad (1)$$

Let C be a nonempty closed convex set². Then, the indicator function $\iota_C \in \Gamma_0(\mathbb{R}^D)$ of C is defined by

$$\iota_C(\mathcal{X}) := \begin{cases} 0, & \text{if } \mathcal{X} \in C; \\ \infty, & \text{otherwise.} \end{cases} \quad (2)$$

¹A convex function is a function $f: \mathbb{R}^D \rightarrow (-\infty, \infty]$ satisfies $f(\lambda\mathcal{X} + (1-\lambda)\mathcal{Y}) \leq \lambda f(\mathcal{X}) + (1-\lambda)f(\mathcal{Y})$ for any $\mathcal{X}, \mathcal{Y} \in \mathbb{R}^D$ and $\lambda \in [0, 1]$. A proper lower-semicontinuous convex function is a convex function such that its domain is nonempty and its level set is closed for any $\alpha \in \mathbb{R}$.

²A set $C \subset \mathbb{R}^D$ is said to be convex if $\lambda\mathcal{X} + (1-\lambda)\mathcal{Y} \in C$ for any $\mathcal{X}, \mathcal{Y} \in C$ and $\lambda \in [0, 1]$.

The proximity operator of an indicator function ι_C equals the metric projection onto C , i.e.,

$$\begin{aligned} \text{prox}_{\gamma\iota_C}(\mathbf{X}) &= \underset{\mathbf{Y} \in C}{\operatorname{argmin}} \iota_C(\mathbf{Y}) + \frac{1}{2\gamma} \|\mathbf{X} - \mathbf{Y}\|_F^2 \\ &= \underset{\mathbf{Y} \in C}{\operatorname{argmin}} \|\mathbf{X} - \mathbf{Y}\|_F =: P_C(\mathbf{X}). \end{aligned} \quad (3)$$

B. Preconditioned Variant of Primal-Dual Splitting Method (P-PDS)

A Primal-Dual Splitting method (PDS) [41] is an efficient algorithm for solving convex optimization problems of the form:

$$\begin{aligned} \min_{\mathbf{x}_1, \dots, \mathbf{x}_N, \mathbf{y}_1, \dots, \mathbf{y}_M} & \sum_{i=1}^N f_i(\mathbf{x}_i) + \sum_{j=1}^M g_j(\mathbf{y}_j), \\ \text{s.t. } & \mathbf{y}_1 = \sum_{i=1}^N \mathcal{L}_{1,i}(\mathbf{x}_i), \dots, \mathbf{y}_M = \sum_{i=1}^N \mathcal{L}_{M,i}(\mathbf{x}_i), \end{aligned} \quad (4)$$

where $f_i \in \Gamma_0(\mathbb{R}^{D_i})$ ($i = 1, \dots, N$) and $g_j \in \Gamma_0(\mathbb{R}^{D_j})$ ($j = 1, \dots, M$) are proximable³ proper lower-semicontinuous convex functions, and $\mathcal{L}_{j,i}$ ($i = 1, \dots, N$, $j = 1, \dots, M$) are linear operators. The stepsizes of the standard PDS must be set manually within a range that satisfies the convergence conditions. On the other hand, Preconditioned variants of PDS (P-PDS) [35]–[37] can automatically determine the appropriate stepsizes based on the problem structure and converge faster in general than the standard PDS. Among them, we adopt P-PDS with Operator-norm-based design method of Variable-wise Diagonal Preconditioning (OVDP) [36], [37]. This method solves Prob. (4) by the following iterative procedures:

$$\begin{aligned} & \mathbf{x}_1^{(n+1)} \leftarrow \text{prox}_{\gamma_{x_1} f_1}(\mathbf{x}_1^{(n)} - \gamma_{x_1}(\sum_{j=1}^M \mathcal{L}_{j,1}^*(\mathbf{y}_j^{(n)}))); \\ & \vdots \\ & \mathbf{x}_N^{(n+1)} \leftarrow \text{prox}_{\gamma_{x_N} f_N}(\mathbf{x}_N^{(n)} - \gamma_{x_N}(\sum_{j=1}^M \mathcal{L}_{j,N}^*(\mathbf{y}_j^{(n)}))); \\ & \tilde{\mathbf{y}}_1 \leftarrow \mathbf{y}_1^{(n)} + \gamma_{y_1}(\sum_{i=1}^N \mathcal{L}_{1,i}(2\mathbf{x}_i^{(n+1)} - \mathbf{x}_i^{(n)})); \\ & \mathbf{y}_1^{(n+1)} \leftarrow \tilde{\mathbf{y}}_1 - \gamma_{y_1} \text{prox}_{\frac{1}{\gamma_{y_1}} g_1}(\frac{1}{\gamma_{y_1}} \tilde{\mathbf{y}}_1); \\ & \vdots \\ & \tilde{\mathbf{y}}_M \leftarrow \mathbf{y}_M^{(n)} + \gamma_{y_M}(\sum_{i=1}^N \mathcal{L}_{M,i}(2\mathbf{x}_i^{(n+1)} - \mathbf{x}_i^{(n)})); \\ & \mathbf{y}_M^{(n+1)} \leftarrow \tilde{\mathbf{y}}_M - \gamma_{y_M} \text{prox}_{\frac{1}{\gamma_{y_M}} g_M}(\frac{1}{\gamma_{y_M}} \tilde{\mathbf{y}}_M); \\ & n \leftarrow n + 1; \end{aligned} \quad (5)$$

where γ_{x_i} ($i = 1, \dots, N$) and γ_{y_j} ($j = 1, \dots, M$) are the stepsizes, which are automatically determined as follows:

$$\gamma_{x_i} = \frac{1}{\sum_{j=1}^M \mu_{j,i}^2}, \quad \gamma_{y_j} = \frac{1}{N}, \quad (6)$$

where $\mu_{j,i}$ ($i = 1, \dots, N$, $j = 1, \dots, M$) are the upper bounds of $\|\mathcal{L}_{j,i}\|_{\text{op}}$ (see Table I for the definition of the operator norm of a linear operator).

III. PROPOSED METHOD

An overview of the proposed method is illustrated in Fig. 1. In this section, to explicitly handle mixed noise superimposed on an HS image, we first introduce an observation model that includes three types of noise. Then, based on the model, we formulate the HS anomaly detection problem as a constrained convex optimization problem and derive a P-PDS-based algorithm to efficiently solve it. Finally, we give several specific designs of functions that characterize a background part, and the computational complexity of the proposed method with each of them.

A. Problem Formulation

We consider the following observation model:

$$\mathbf{V} = \mathbf{B} + \mathbf{A} + \mathbf{S} + \mathbf{L} + \mathbf{N}, \quad (7)$$

where $\mathbf{V} \in \mathbb{R}^{H \times W \times B}$ is a given HS image (H and W are the height and width of the HS image, and B is the number of the spectral bands), $\mathbf{B} \in \mathbb{R}^{H \times W \times B}$ is a background part, $\mathbf{A} \in \mathbb{R}^{H \times W \times B}$ is an anomaly part, $\mathbf{S} \in \mathbb{R}^{H \times W \times B}$ is sparse noise, $\mathbf{L} \in \mathbb{R}^{H \times W \times B}$ is stripe noise, and $\mathbf{N} \in \mathbb{R}^{H \times W \times B}$ is Gaussian noise.

Based on this model, we formulate the HS anomaly detection problem with mixed noise removal as the following constrained convex optimization problem:

$$\begin{aligned} \min_{\mathbf{B}, \mathbf{A}, \mathbf{S}, \mathbf{L}} & R(\mathcal{L}(\mathbf{B})) + \lambda_1 \|\mathbf{A}\|_{2,1} + \lambda_2 \|\mathbf{L}\|_1, \\ \text{s.t. } & \begin{cases} \mathcal{D}_v(\mathbf{L}) = \mathcal{O}, \\ \mathbf{B} + \mathbf{A} + \mathbf{S} + \mathbf{L} \in \mathcal{B}_{F,\varepsilon}^{\mathbf{V}}, \\ \mathbf{S} \in \mathcal{B}_{1,\alpha}, \end{cases} \end{aligned} \quad (8)$$

where $\lambda_1 \geq 0$ and $\lambda_2 \geq 0$ are hyperparameters. Here, R is a non-differentiable convex function whose proximity operator can be computed efficiently, and \mathcal{L} is a linear operator. For the definitions of $\mathcal{B}_{F,\varepsilon}^{\mathbf{V}}$ and $\mathcal{B}_{1,\alpha}$, see Table I. The role of each term and constraint in Prob. (8) is summarized as follows:

- The first term is a general form of a suitably-chosen function to characterize the spatial continuity and/or the spectral correlation of the background part. We introduce some specific examples of the function design in Sec. III-C.
- The second term models the spatial sparsity of the anomaly part. This is based on the fact that anomalies are small objects with a low probability of existence in the spatial domain.
- The third term and the first constraint characterize stripe noise that is superimposed with constant intensity in one direction. In this article, without loss of generality, we assume that this noise is generated only in the vertical direction. Specifically, the third term adjusts the sparsity of stripe noise, while the first constraint, called the flatness constraint, models the constant intensity. The advantages of such characterizations for stripe noise are described in [42].

³If the proximity operator of a function $f \in \Gamma_0(\mathbb{R}^D)$ is efficiently computable, we call f *proximable*.

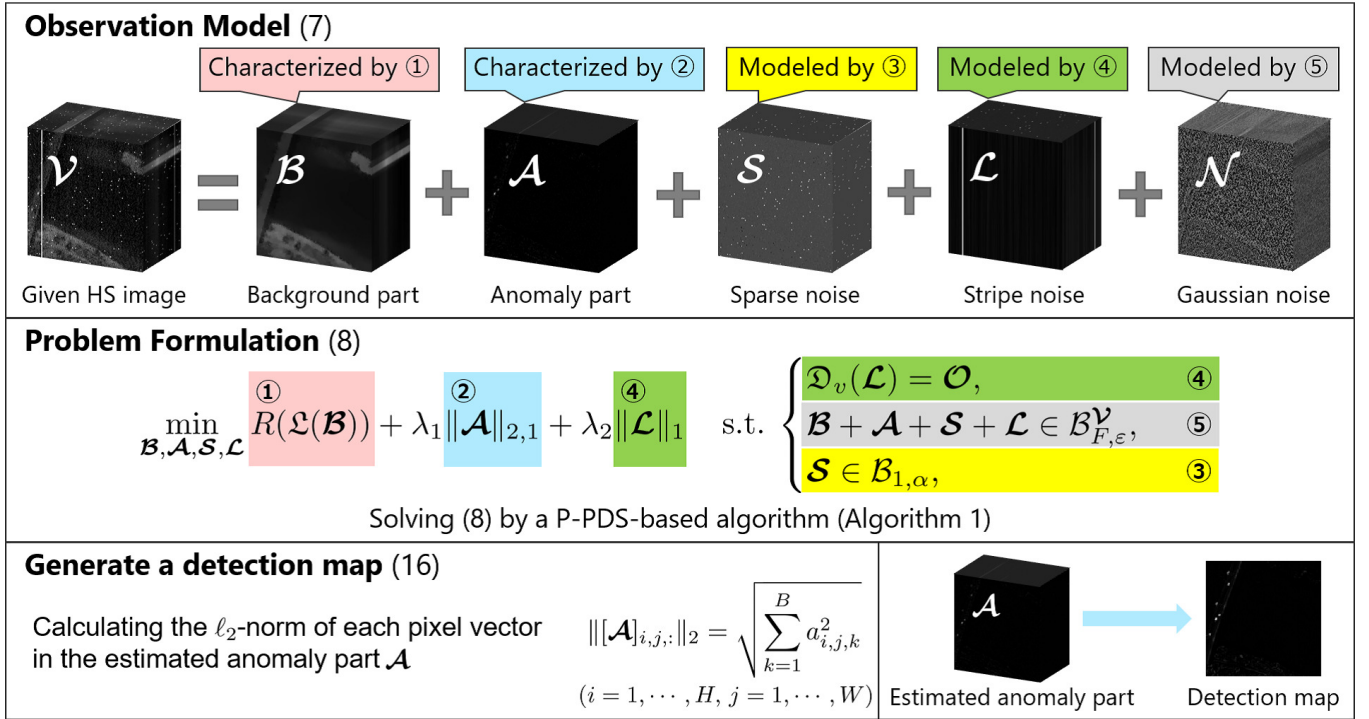


Fig. 1. Overview of the proposed method.

- The second constraint serves as a data-fidelity to the given HS image, where the upper bound ε of the Frobenius norm is adjusted based on the intensity of Gaussian noise.
- The third constraint models sparse noise, where the upper bound α of the ℓ_1 -norm is adjusted based on the probability of its occurrence. Unlike anomalies, sparse noise is not continuous in the spectral direction and occurs irregularly, and thus we estimate each separately.

B. Optimization Algorithm

We develop an efficient solver for Prob. (8) based on P-PDS with OVPD [36], [37]. First, using the indicator functions $\iota_{\mathcal{B}_{1,\alpha}}$, $\iota_{\mathcal{B}_{F,\varepsilon}^V}$, and $\iota_{\{\mathcal{O}\}}$ (see Eq. (2) for the definition), we rewrite Prob. (8) as the following equivalent problem:

$$\begin{aligned}
 & \min_{\substack{\mathcal{B}, \mathcal{A}, \mathcal{S}, \mathcal{L}, \\ \mathcal{Y}_1, \mathcal{Y}_2, \mathcal{Y}_3}} R(\mathcal{Y}_1) + \lambda_1 \|\mathcal{A}\|_{2,1} + \lambda_2 \|\mathcal{L}\|_1 \\
 & \quad + \iota_{\{\mathcal{O}\}}(\mathcal{Y}_2) + \iota_{\mathcal{B}_{F,\varepsilon}^V}(\mathcal{Y}_3) + \iota_{\mathcal{B}_{1,\alpha}}(\mathcal{S}), \\
 & \text{s.t.} \quad \begin{cases} \mathcal{Y}_1 = \mathcal{L}(\mathcal{B}), \\ \mathcal{Y}_2 = \mathcal{D}_v(\mathcal{L}), \\ \mathcal{Y}_3 = \mathcal{B} + \mathcal{A} + \mathcal{S} + \mathcal{L}, \end{cases} \quad (9)
 \end{aligned}$$

where \mathcal{Y}_1 , \mathcal{Y}_2 and \mathcal{Y}_3 are auxiliary variables. Then, by defining,

$$\begin{aligned}
 f_1(\mathcal{B}) &:= 0, \quad f_2(\mathcal{A}) := \lambda_1 \|\mathcal{A}\|_{2,1}, \\
 f_3(\mathcal{S}) &:= \iota_{\mathcal{B}_{1,\alpha}}(\mathcal{S}), \quad f_4(\mathcal{L}) := \lambda_2 \|\mathcal{L}\|_1, \\
 g_1(\mathcal{Y}_1) &:= R(\mathcal{Y}_1), \quad g_2(\mathcal{Y}_2) := \iota_{\{\mathcal{O}\}}(\mathcal{Y}_2), \\
 g_3(\mathcal{Y}_3) &:= \iota_{\mathcal{B}_{F,\varepsilon}^V}(\mathcal{Y}_3), \quad (10)
 \end{aligned}$$

Prob. (9) can be seen as Prob. (4), so that we can apply P-PDS with OVPD to Prob. (9). We show the detailed algorithm in Algorithm 1. Following Eq. (6), the stepsizes γ_B , γ_A , γ_S , γ_L , γ_{Y_1} , γ_{Y_2} , γ_{Y_3} are automatically determined as follows:

$$\begin{aligned}
 \gamma_B &= \frac{1}{1 + \|\mathcal{D}_v\|_{\text{op}}^2}, \quad \gamma_A = 1, \quad \gamma_S = 1, \quad \gamma_L = \frac{1}{5}, \\
 \gamma_{Y_1} &= \gamma_{Y_2} = \gamma_{Y_3} = \frac{1}{4}. \quad (11)
 \end{aligned}$$

In what follows, we explain how to compute each step of Algorithm 1. The computations of the proximity operators of the $\ell_{2,1}$ -norm in Step 4 and the ℓ_1 -norm in Step 6 are given as follows:

$$[\text{prox}_{\gamma \|\cdot\|_{2,1}}(\mathcal{X})]_{i,j,k} = \max\left\{1 - \frac{\gamma}{\|[\mathcal{X}]_{i,j,:}\|_2}, 0\right\} [\mathcal{X}]_{i,j,k}, \quad (12)$$

$$[\text{prox}_{\gamma \|\cdot\|_1}(\mathcal{X})]_{i,j,k} = \text{sgn}([\mathcal{X}]_{i,j,k}) \max\{|[\mathcal{X}]_{i,j,k}| - \gamma, 0\}. \quad (13)$$

In addition, the proximity operators of $\iota_{\{\mathcal{O}\}}$ in Step 10 and $\iota_{\mathcal{B}_{F,\varepsilon}^V}$ in Step 12 are the metric projections onto \mathcal{O} and $\mathcal{B}_{F,\varepsilon}^V$, respectively. Their computations are given by

$$\text{prox}_{\gamma \iota_{\{\mathcal{O}\}}}(\mathcal{X}) = P_{\{\mathcal{O}\}}(\mathcal{X}) = \mathcal{O}, \quad (14)$$

$$\begin{aligned}
 \text{prox}_{\gamma \iota_{\mathcal{B}_{F,\varepsilon}^V}}(\mathcal{X}) &= P_{\mathcal{B}_{F,\varepsilon}^V}(\mathcal{X}) \\
 &= \begin{cases} \mathcal{X}, & \text{if } \mathcal{X} \in \mathcal{B}_{F,\varepsilon}^V; \\ \mathcal{Y} + \frac{\varepsilon(\mathcal{X} - \mathcal{Y})}{\|\mathcal{X} - \mathcal{Y}\|_F}, & \text{otherwise.} \end{cases} \quad (15)
 \end{aligned}$$

For the computation of the proximity operator of $\iota_{\mathcal{B}_{1,\alpha}}$ in Step 5, we use a fast ℓ_1 -ball projection algorithm [43].

Algorithm 1 Proposed algorithm for solving Prob. (8)

Input: \mathbf{V} , λ_1 , λ_2 , ε , α
Initialize: $\mathbf{B}^{(0)} = \mathbf{O}$, $\mathbf{A}^{(0)} = \mathbf{O}$, $\mathbf{S}^{(0)} = \mathbf{O}$, $\mathbf{L}^{(0)} = \mathbf{O}$,
 $\mathbf{Y}_1^{(0)} = \mathbf{O}$, $\mathbf{Y}_2^{(0)} = \mathbf{O}$, $\mathbf{Y}_3 = \mathbf{O}$, γ_B , γ_A , γ_S , γ_L , γ_{Y_1} ,
 γ_{Y_2} , γ_{Y_3}
1: $n = 0$;
2: **while** stopping conditions are not met, **do**
3: $\mathbf{B}^{(n+1)} \leftarrow \mathbf{B}^{(n)} - \gamma_B (\mathbf{L}^*(\mathbf{Y}_1^{(n)}) + \mathbf{Y}_3^{(n)})$;
4: $\mathbf{A}^{(n+1)} \leftarrow \text{prox}_{\gamma_A \lambda_1 \|\cdot\|_{2,1}}(\mathbf{A}^{(n)} - \gamma_A \mathbf{Y}_3^{(n)})$;
5: $\mathbf{S}^{(n+1)} \leftarrow P_{\mathbf{B}_{1,\alpha}}(\mathbf{S}^{(n)} - \gamma_S \mathbf{Y}_3^{(n)})$;
6: $\mathbf{L}^{(n+1)} \leftarrow \text{prox}_{\gamma_L \lambda_2 \|\cdot\|_1}(\mathbf{L}^{(n)} - \gamma_L (\mathbf{D}_v^*(\mathbf{Y}_2^{(n)}) + \mathbf{Y}_3^{(n)}))$;
7: $\tilde{\mathbf{Y}}_1 \leftarrow \mathbf{Y}_1^{(n)} + \gamma_{Y_1} \mathbf{L}(2\mathbf{B}^{(n+1)} - \mathbf{B}^{(n)})$;
8: $\mathbf{Y}_1^{(n+1)} \leftarrow \tilde{\mathbf{Y}}_1 - \gamma_{Y_1} \text{prox}_{\frac{1}{\gamma_{Y_1}} R}(\frac{\tilde{\mathbf{Y}}_1}{\gamma_{Y_1}})$;
9: $\tilde{\mathbf{Y}}_2 \leftarrow \mathbf{Y}_2^{(n)} + \gamma_{Y_2} \mathbf{D}_v(2\mathbf{L}^{(n+1)} - \mathbf{L}^{(n)})$;
10: $\mathbf{Y}_2^{(n+1)} \leftarrow \tilde{\mathbf{Y}}_2 - \gamma_{Y_2} P_{\{\mathbf{O}\}}(\frac{\tilde{\mathbf{Y}}_2}{\gamma_{Y_2}})$;
11: $\tilde{\mathbf{Y}}_3 \leftarrow \mathbf{Y}_3^{(n)} + \gamma_{Y_3} (2(\mathbf{B}^{(n+1)} + \mathbf{A}^{(n+1)} + \mathbf{S}^{(n+1)} + \mathbf{L}^{(n+1)}) - (\mathbf{B}^{(n)} + \mathbf{A}^{(n)} + \mathbf{S}^{(n)} + \mathbf{L}^{(n)}))$;
12: $\mathbf{Y}_3^{(n+1)} \leftarrow \tilde{\mathbf{Y}}_3 - \gamma_{Y_3} P_{\mathbf{B}_{F,\varepsilon}}(\frac{\tilde{\mathbf{Y}}_3}{\gamma_{Y_3}})$;
13: $n \leftarrow n + 1$;
14: **end while**
Output: $\mathbf{B}^{(n)}$, $\mathbf{A}^{(n)}$, $\mathbf{S}^{(n)}$, $\mathbf{L}^{(n)}$

After estimating the anomaly part \mathbf{A} , we generate a 2D detection map by calculating the ℓ_2 -norm of each pixel vector as follows:

$$\|[\mathbf{A}]_{i,j,:}\|_2 = \sqrt{\sum_{k=1}^B a_{i,j,k}^2}, \quad (i = 1, \dots, H, j = 1, \dots, W). \quad (16)$$

C. Specific Designs of Background Characterization Function

We give some examples of $R(\mathbf{L}(\mathbf{B}))$ that characterizes the background part in Prob. (8).

1) *Hyperspectral Total Variation (HTV)* [44]: HTV models the spatial piecewise smoothness of the background part by promoting the group sparsity of vertical and horizontal neighborhood differences across all bands. We define a spatial difference operator as

$$[\mathbf{D}(\mathbf{X})]_{i,j,k} := \begin{cases} [\mathbf{D}_v(\mathbf{X})]_{i,j,k}, & (1 \leq k \leq d_3), \\ [\mathbf{D}_h(\mathbf{X})]_{i,j,k-d_3}, & (d_3 < k \leq 2d_3), \end{cases} \quad (17)$$

where \mathbf{D}_v and \mathbf{D}_h denote the vertical and horizontal difference operators, respectively (see Table I for more details). The definition of HTV is given by

$$\|\mathbf{X}\|_{\text{HTV}} := \|\mathbf{D}(\mathbf{X})\|_{2,1}. \quad (18)$$

Then, we can see that HTV is a special case of $R(\mathbf{L}(\mathbf{B}))$ by letting $R = \|\cdot\|_{2,1}$ and $\mathbf{L} = \mathbf{D}$. Note that the computation of the proximity operator of the $\ell_{2,1}$ -norm is shown in Eq. (12).

2) *Spatio-Spectral Total Variation (SSTV)* [45]: SSTV can promote the spatial and spectral piecewise smoothness of the background part. SSTV is defined, by using the vertical and horizontal differences of spectral differences, as

$$\|\mathbf{X}\|_{\text{SSTV}} := \|\mathbf{D}(\mathbf{D}_b(\mathbf{X}))\|_1, \quad (19)$$

where \mathbf{D}_b denotes the spectral difference operator (see Table I for the definition). Then, we can see that SSTV is a special case of $R(\mathbf{L}(\mathbf{B}))$ by letting $R = \|\cdot\|_1$ and $\mathbf{L} = \mathbf{D} \circ \mathbf{D}_b$. Note that the computation of the proximity operator of the ℓ_1 -norm is shown in Eq. (13).

3) *Hybrid Spatio-Spectral Total Variation (HSSTV)* [46]: HSSTV is a hybrid of HTV and SSTV. We define a spatial-spectral difference operator as

$$[\mathbf{A}_\omega(\mathbf{X})]_{i,j,k} := \begin{cases} [\mathbf{D}(\mathbf{D}_b(\mathbf{X}))]_{i,j,k}, & (1 \leq k \leq 2d_3), \\ \omega [\mathbf{D}(\mathbf{X})]_{i,j,k-2d_3}, & (2d_3 < k \leq 4d_3), \end{cases} \quad (20)$$

where $\omega > 0$ is a hyperparameter. Then, HSSTV is defined by

$$\|\mathbf{X}\|_{\text{HSSTV}} := \|\mathbf{A}_\omega(\mathbf{X})\|_1. \quad (21)$$

Here, we can see that HSSTV is a special case of $R(\mathbf{L}(\mathbf{B}))$ by letting $R = \|\cdot\|_1$ and $\mathbf{L} = \mathbf{A}_\omega$. The computation of the proximity operator of the ℓ_1 -norm is shown in Eq. (13).

4) *Nuclear Norm*: Due to the high spectral correlation between background pixels, the background part exhibits low-rank characteristics. To model this, we can also use a low-rank approximation using the nuclear norm. For $\mathbf{X} \in \mathbb{R}^{M \times N}$ ($M \leq N$), the nuclear norm of \mathbf{X} is given by

$$\|\mathbf{X}\|_* := \sum_{i=1}^M \sigma_i(\mathbf{X}), \quad (22)$$

where $\sigma_i(\cdot)$ is the i -th largest singular value of \mathbf{X} . Here, we define $\text{mat}(\mathbf{X}) : \mathbb{R}^{H \times W \times B} \rightarrow \mathbb{R}^{B \times HW}$ as an operator that reshapes a three-dimensional HS image cube into a matrix. Then, we can see that the nuclear norm is a special case of $R(\mathbf{L}(\mathbf{B}))$ by letting $R = \|\cdot\|_*$ and $\mathbf{L} = \text{mat}$.

Let the singular value decomposition of $\mathbf{X} \in \mathbb{R}^{M \times N}$ ($M \leq N$) be $\mathbf{X} = \mathbf{U}\mathbf{\Sigma}\mathbf{V}^\top$. The computation of the proximity operator of the nuclear norm is given as follows:

$$\text{prox}_{\gamma \|\cdot\|_*}(\mathbf{X}) = \mathbf{U}\tilde{\mathbf{\Sigma}}_\gamma \mathbf{V}^\top, \quad (23)$$

where $\tilde{\mathbf{\Sigma}}_\gamma$ is a diagonal matrix whose diagonal elements are given by $[\text{diag}(\tilde{\mathbf{\Sigma}}_\gamma)]_i = \max\{\sigma_i(\mathbf{X}) - \gamma, 0\}$ for $i = 1, \dots, M$.

5) *Stepsize Choices for Each Background Characterization*: Finally, we derive the choices of the stepsize γ_B in Eq. (11) for each background characterization. The operator norm of the identity operator is 1. In addition, from [47], each difference operator satisfies $\|\mathbf{D}_v\|_{\text{op}} \leq 2$, $\|\mathbf{D}_h\|_{\text{op}} \leq 2$, $\|\mathbf{D}_b\|_{\text{op}} \leq 2$, and $\|\mathbf{D}\|_{\text{op}} \leq 2\sqrt{2}$, respectively. Furthermore, from the submultiplicity of the operator norm, we have $\|\mathbf{D} \circ \mathbf{D}_b\|_{\text{op}} \leq \|\mathbf{D}\|_{\text{op}} \|\mathbf{D}_b\|_{\text{op}} \leq 4\sqrt{2}$. Substituting these values and upper bounds into Eq. (6), we can determine the stepsize γ_B as shown in Table II.

TABLE II
SPECIFIC FUNCTION R , LINEAR OPERATOR \mathfrak{L} , AND STEPSIZE γ_B WITH
RESPECT TO EACH BACKGROUND CHARACTERIZATION.

Regularizations	R	\mathfrak{L}	γ_B in Eq. (11)
HTV [44]	$\ \cdot\ _{2,1}$	\mathfrak{D}	$\frac{1}{9}$
SSTV [45]	$\ \cdot\ _1$	$\mathfrak{D} \circ \mathfrak{D}_b$	$\frac{1}{33}$
HSSTV [46]	$\ \cdot\ _1$	\mathfrak{A}_ω	$\frac{1}{33+8\omega^2}$
Nuclear Norm	$\ \cdot\ _*$	mat	$\frac{1}{2}$

TABLE III
COMPUTATIONAL COMPLEXITY OF EACH OPERATION.

Operations	\mathcal{O} -notations
$\mathfrak{D}(\mathcal{X})$	$\mathcal{O}(N)$
$\mathfrak{D}(\mathfrak{D}_b(\mathcal{X}))$	$\mathcal{O}(N)$
$\mathfrak{A}_\omega(\mathcal{X})$	$\mathcal{O}(N)$
$\text{prox}_{\gamma\ \cdot\ _{2,1}}(\mathcal{X})$ in (12)	$\mathcal{O}(N)$
$\text{prox}_{\gamma\ \cdot\ _1}(\mathcal{X})$ in (13)	$\mathcal{O}(N)$
$P_{\mathcal{B}_{F,\varepsilon}}(\mathcal{X})$ in (15)	$\mathcal{O}(N)$
$P_{\{\mathcal{O}\}}(\mathcal{X})$ in (14)	$\mathcal{O}(1)$
$P_{\mathcal{B}_{1,\alpha}}(\mathcal{X})$ in [43]	$\mathcal{O}(N \log N)$
$\text{prox}_{\gamma\ \cdot\ _*}(\mathbf{X})$ in (23)	$\mathcal{O}(BN)$

D. Computational Complexity

Table III shows the computational complexity of the operation for a tensor $\mathcal{X} \in \mathbb{R}^{H \times W \times B}$ and a matrix $\mathbf{X} \in \mathbb{R}^{B \times HW}$ used in the proposed method. Let $N = HWB$, the computational complexity for each step of Algorithm 1 is as follows:

- Steps 3, 4, 6, 7, 9, 11 and 12: $\mathcal{O}(N)$.
- Step 5: $\mathcal{O}(N \log N)$.
- Step 10: $\mathcal{O}(1)$.
- Step 8: $\mathcal{O}(N)$ when HTV, SSTV, or HSSTV is used to characterize the background part; and $\mathcal{O}(BN)$ when the nuclear norm is used.

From the above, the overall computational complexity for each iteration of the proposed method using HTV, SSTV, or HSSTV is $\mathcal{O}(N \log N)$, and since $\log N \ll B$ in general, the proposed method using the nuclear norm is $\mathcal{O}(BN)$.

IV. EXPERIMENTS

In this section, we demonstrate the effectiveness of the proposed method through comprehensive experiments using a number of HS anomaly detection datasets. Specifically, we verify the following two points:

- The proposed method achieves state-of-the-art detection performance in noise-free cases.
- The proposed method is much more robust against various types of noise than existing methods.

All experiments were conducted using MATLAB R2021a on a 64-bit Windows 10 PC with an Intel Core i9-10900K, 32GB of RAM, and an NVIDIA GeForce RTX 3090.

TABLE IV
DETAILS OF THE HS IMAGES USED IN THE EXPERIMENT.

Data	Sensor	Time	Resolution	Size
Pavia Centre	ROSIS-03	—	1.3 m	$150 \times 150 \times 102$
Texas Coast	AVIRIS	Aug. 29, 2010	17.2 m	$100 \times 100 \times 204$
Gainesville	AVIRIS	Sep. 4, 2010	3.5 m	$100 \times 100 \times 191$
Los Angeles I	AVIRIS	Nov. 9, 2011	7.1 m	$100 \times 100 \times 205$
Los Angeles II	AVIRIS	Nov. 9, 2011	7.1 m	$100 \times 100 \times 205$
San Diego	AVIRIS	—	3.5 m	$100 \times 100 \times 189$

TABLE V
NOISE SETTING. HERE, σ IS THE STANDARD DEVIATION OF GAUSSIAN NOISE, S_p AND S_l ARE SALT-AND-PEPPER AND STRIPE NOISE RATES, RESPECTIVELY. NOTE THAT THE INTENSITY OF STRIPE NOISE IS UNIFORMLY RANDOM IN THE RANGE $[-0.3, 0.3]$, AND "—" INDICATES THAT NO NOISE WAS ADDED.

Cases	Gaussian	salt-and-pepper	stripe
Case 1	—	—	—
Case 2	$\sigma = 0.03$	—	—
Case 3	—	$S_p = 0.03$	$S_l = 0.03$
Case 4	$\sigma = 0.01$	$S_p = 0.01$	$S_l = 0.01$
Case 5	$\sigma = 0.05$	$S_p = 0.05$	$S_l = 0.05$

TABLE VI
HYPERPARAMETER SETTINGS IN EACH METHOD.

Methods	Parameters
LRX [9], 2S-GLRT [13]	$\omega_{in} = [3, 5, 7, 9, 11, 13, 15]$, $\omega_{out} = [5, 7, 9, 11, 13, 15, 17, 19, 21, 23, 25]$
RGAE [28]	$n_{hid} = [20, 40, 60, 80, 100, 120, 140, 160]$, $S = [50, 100, 150, 300, 500]$, $\lambda = [10^{-4}, 10^{-3}, 10^{-2}, 10^{-1}]$
CRD [16]	$\lambda = 10^{-6}$, $\omega_{in} = [3, 5, 7, 9, 11, 13, 15]$, $\omega_{out} = [5, 7, 9, 11, 13, 15, 17, 19, 21, 23, 25]$
RPCA-RX [18]	$\lambda = [10^{-4}, 10^{-3}, 10^{-2}, 10^{-1}, 10^0, 10^1, 10^2, 10^3, 10^4]$
GTVLRR [21]	$M = 6$, $P = 20$, $\lambda = [0.005, 0.05, 0.1, 0.3, 0.5, 0.7, 1]$, $\beta = [0.005, 0.05, 0.1, 0.2, 0.4, 0.7, 1]$, $\gamma = [0.005, 0.01, 0.02, 0.05, 0.1, 0.2, 0.5]$
LSDM-MoG [22]	$t_0 = 10^{-3}$, $\mu_0 = 0$, $\alpha_{01}, \dots, \alpha_{0K}, \beta_0, a_0, b_0, c_0, d_0 = 10^{-6}$, $l_0 = [10, 20, 30, 40, 50, 60, 70, 80, 90, 100]$, $K = [1, 2, 3, 4, 5, 6, 7, 8, 9, 10]$
Ours (HTV)	$\lambda_1 = [0.01, 0.05, 0.1, 0.25, 0.5, 0.75, 1, 1.5, 2]$, $\lambda_2 = [0, 0.001, 0.01, 0.025, 0.05, 0.075, 0.1, 0.25, 0.5, 1]$
Ours (SSTV)	$\lambda_1 = [0.1, 0.25, 0.5, 0.75, 1, 1.25, 1.5, 5, 10]$, $\lambda_2 = [0, 0.001, 0.01, 0.025, 0.05, 0.075, 0.1, 0.25, 0.5, 1]$
Ours (HSSTV)	$\omega = 0.05$, $\lambda_1 = [0.05, 0.1, 0.25, 0.5, 0.75, 1, 1.25, 1.5, 2]$, $\lambda_2 = [0, 0.001, 0.005, 0.0075, 0.01, 0.025, 0.05, 0.1, 0.5, 1]$
Ours (Nuclear)	$\lambda_1 = [0.005, 0.01, 0.025, 0.05, 0.075, 0.1, 0.25, 0.5, 1]$, $\lambda_2 = [0, 0.001, 0.01, 0.025, 0.05, 0.075, 0.1, 0.25, 0.5, 1]$

A. Experimental Setup

We used six HS anomaly detection datasets from [48]. Fig. 2 shows the pseudocolor images and ground truths of these datasets. The details of each dataset are shown in Table IV.

We compare the proposed method with eight existing HS anomaly detection methods from classical to state-of-the-art ones. Specifically, we adopted the statistics-based methods: Global Reed-Xiaoli Detector (GRX) [8], Local Reed-Xiaoli Detector (LRX) [9], and Two-Step Generalized Likelihood

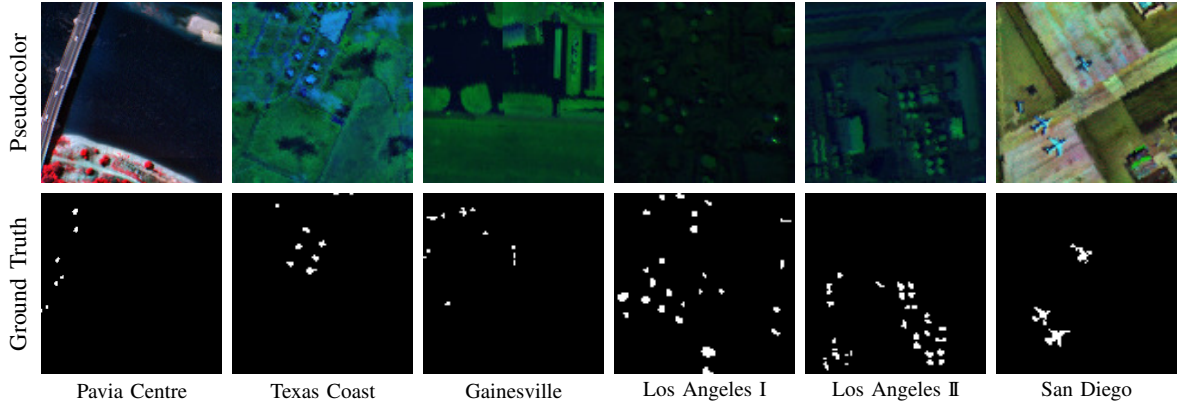


Fig. 2. Pseudocolor images and ground truths for each dataset.

Ratio Test (2S-GLRT) [13]; the representation-based method: Collaborative-Representation based Detector (CRD) [16]; the decomposition-based methods: Robust Principal Component Analysis with Reed-Xiaoli Detector (RPCA-RX) [18], Graph and Total Variation regularized Low-Rank Representation (GTVLRR) [21], and Low-rank and Sparse Decomposition with Mixture of Gaussian (LSDM-MoG) [22]; and the deep learning-based method: Robust Graph AE (RGAE) [28].

To evaluate the detection performance of the existing and proposed methods in various scenarios, we consider the five noise contamination cases shown in Table V in our experiments. Briefly, Case 1 corresponds to a noise-free scenario, Case 2 assumes a given HS image contains only Gaussian noise, and the other cases handle different scenarios of mixed noise contamination.

B. Evaluation Metrics

We adopt the following two metrics for evaluating the detection performance: Area Under the receiver operating characteristic (ROC) Curve (AUC) [49] and Square Error Ratio (SER) [50].

1) *Area Under the Curve (AUC)* [49]: AUC is the area under the ROC curve with the false positive rate P_{FA} plotted on the horizontal axis and the true positive rate P_D on the vertical axis. Here, P_D and P_{FA} can be calculated for each threshold as follows:

$$P_D = \frac{N_{AA}}{N_A}, \quad P_{FA} = \frac{N_{BA}}{N_B}, \quad (24)$$

where N_{AA} and N_{BA} are the total number of anomaly and background pixels with values higher than the threshold, respectively, and N_A and N_B are the total number of anomaly and background pixels, respectively. The closer the ROC curve is to the upper left, i.e., the closer the AUC value is to 1, the better the detection performance.

2) *Squared Error Ratio (SER)* [50]: SER is a measure of the squared error between the ground truth (GT) and the detection map and is calculated as follows:

$$\text{SER} = \frac{\sum_{i=1}^{N_A} (p_i - 1)^2 + \sum_{j=1}^{N_B} (p_j - 0)^2}{N_A + N_B} \times 100, \quad (25)$$

where p_i and p_j are the anomaly and background pixel values of the detection map normalized to $[0, 1]$, respectively. The smaller the SER value, the better the detection accuracy.

C. Parameter Setting

The hyperparameters of each method used in the experiments were set to the value that maximized the AUC value after examining the AUC values in the range shown in Table VI.

For the proposed method, we set the stopping condition for Algorithm 1 to

$$\frac{\|\mathcal{T}^{(n+1)} - \mathcal{T}^{(n)}\|_F}{\|\mathcal{T}^{(n)}\|_F} \leq 10^{-5}, \quad (26)$$

where $\mathcal{T}^{(n)} = \mathcal{B}^{(n)} + \mathcal{A}^{(n)} + \mathcal{S}^{(n)} + \mathcal{L}^{(n)}$, and the maximum number of iterations to 10,000 for the proposed method using HTV, SSTV, or HSSTV and 5,000 for the proposed method using the nuclear norm. We also set ε and α in Prob. (8) as

$$\varepsilon = \eta\sigma\sqrt{HWB(1 - S_p)}, \quad \alpha = \frac{1}{2}\eta S_p HWB, \quad (27)$$

with $\eta = 0.9$, respectively.

D. Experimental Results

1) *Case 1 (Noise-free)*: Tables VII and VIII show the AUC and SER values of all the detectors for each dataset, respectively. The best and second-best results are highlighted in bold and underlined, respectively. Surprisingly, the detection performance of the proposed method is comparable to the existing state-of-the-art methods, even though, it does not use a background dictionary and only uses HTV, SSTV, HSSTV, or the nuclear norm to characterize the background part. In particular, the proposed method using HTV achieved the best AUC and SER values on most datasets. This indicates that evaluating the spatial continuity of the background part only by the difference between neighboring pixels improves the detection performance.

Fig. 4 shows the detection maps for Pavia Centre generated by all the detectors. CRD and LSDM-MoG detected all anomalies, but there are some regions where they failed to distinguish between background and anomalies. On the

TABLE VII
AUC VALUES OF ALL THE DETECTORS FOR EACH DATASET.
(THE BEST AND SECOND-BEST AUC VALUES ARE HIGHLIGHTED IN BOLD AND UNDERLINED, RESPECTIVELY.)

Datasets	Noise	Methods											
		GRX [8]	LRX [9]	2S-GLRT [13]	RGAE [28]	CRD [16]	RPCA-RX [18]	GTVLRR [21]	LSDM-MoG [22]	Ours (HTV)	Ours (SSTV)	Ours (HSSTV)	Ours (Nuclear)
Pavia Centre	Case 1	0.9538	0.9597	0.9868	0.9166	0.9407	0.9591	0.9829	0.9603	0.9908	0.9739	0.9872	0.9673
	Case 2	0.9188	0.9591	0.9935	0.9157	0.9435	0.9188	0.9799	0.7996	<u>0.9889</u>	0.9752	0.9865	0.9389
	Case 3	0.5739	0.7117	0.6411	0.8756	0.7980	0.5753	0.8543	0.8267	0.9910	0.9800	<u>0.9864</u>	0.9428
	Case 4	0.6451	0.7791	0.7300	0.8937	0.7042	0.6456	0.9041	0.7625	0.9903	0.9801	<u>0.9867</u>	0.9389
	Case 5	0.4904	0.7770	0.6530	0.8072	0.7583	0.4904	0.7497	0.8975	0.9784	0.9505	<u>0.9723</u>	0.9109
Texas Coast	Case 1	0.9907	0.9969	<u>0.9970</u>	0.9827	0.9936	0.9926	0.9881	0.9958	0.9978	0.9896	0.9949	0.9965
	Case 2	0.9016	0.9847	0.9850	0.9821	0.9906	0.9026	0.9879	0.8252	0.9971	0.9867	0.9945	0.9886
	Case 3	0.5662	0.8684	0.8021	0.9364	0.7225	0.5667	0.9108	0.8269	0.9979	0.9878	<u>0.9961</u>	0.9884
	Case 4	0.5277	0.9145	0.9541	0.9538	0.6494	0.5318	0.9137	0.7063	0.9978	0.9892	<u>0.9954</u>	0.9881
	Case 5	0.5499	0.8903	0.9494	0.8819	0.7342	0.5502	0.7910	0.8355	0.9953	0.9882	<u>0.9922</u>	0.9841
Gainesville	Case 1	0.9513	0.9769	0.9486	0.8219	0.9393	0.9586	<u>0.9926</u>	0.9838	0.9950	0.9827	0.9881	0.9765
	Case 2	0.7806	0.9562	0.9472	0.8340	0.9206	0.7836	0.9312	0.7458	0.9951	0.9629	<u>0.9878</u>	0.9556
	Case 3	0.4659	0.8530	0.7775	0.6162	0.5612	0.4662	0.5211	0.6450	0.9936	0.9570	<u>0.9861</u>	0.9398
	Case 4	0.5857	0.8857	0.8695	0.7537	0.6551	0.5869	0.9468	0.6865	0.9952	0.9703	<u>0.9884</u>	0.9636
	Case 5	0.5312	0.7555	0.7539	0.6299	0.6276	0.5312	0.5926	0.6126	0.9824	0.9222	<u>0.9728</u>	0.9232
Los Angeles I	Case 1	0.9887	0.9680	0.9265	0.9948	0.9681	0.9887	0.9923	0.9950	<u>0.9964</u>	0.9965	0.9965	0.9963
	Case 2	0.7863	0.9695	0.9712	0.9922	0.9149	0.7863	0.9967	0.5614	0.9929	0.9892	0.9931	0.9962
	Case 3	0.5224	0.7585	0.6460	0.6901	0.5720	0.5234	0.8686	0.8138	0.9954	0.9891	0.9964	0.9961
	Case 4	0.5507	0.8007	0.8150	0.8146	0.5785	0.5514	0.9719	0.6941	0.9958	0.9897	<u>0.9964</u>	0.9966
	Case 5	0.4823	0.6207	0.7396	0.6174	0.5309	0.4823	0.8403	0.8846	<u>0.9864</u>	0.9588	0.9840	0.9943
Los Angeles II	Case 1	0.9692	0.9523	0.9406	0.9572	0.9026	0.9692	0.9290	0.9613	0.9890	0.9830	<u>0.9861</u>	0.9637
	Case 2	0.7111	0.9274	0.9406	0.9545	0.8880	0.7129	0.9502	0.5771	0.9845	0.9777	<u>0.9829</u>	0.9618
	Case 3	0.4752	0.7687	0.6938	0.8684	0.5507	0.4765	0.6466	0.8162	0.9879	0.9786	<u>0.9853</u>	0.9619
	Case 4	0.5372	0.7770	0.7573	0.9122	0.5859	0.5383	0.7272	0.6270	0.9876	0.9827	<u>0.9864</u>	0.9647
	Case 5	0.4808	0.7962	0.8256	0.8234	0.6574	0.4808	0.6410	0.8522	0.9796	0.9740	<u>0.9785</u>	0.9610
San Diego	Case 1	0.9403	0.8797	0.9074	<u>0.9921</u>	0.9814	0.9478	0.9927	0.9709	0.9866	0.9616	0.9700	0.9816
	Case 2	0.8461	0.9569	0.9529	<u>0.9902</u>	0.8919	0.8701	0.9916	0.7374	0.9852	0.9601	0.9807	0.9641
	Case 3	0.5544	0.7973	0.6046	0.8218	0.7041	0.5583	0.8844	0.6888	0.9878	0.9459	<u>0.9832</u>	0.9614
	Case 4	0.5719	0.7932	0.7756	0.8890	0.6578	0.5760	0.9315	0.6626	0.9865	0.9760	<u>0.9814</u>	0.9712
	Case 5	0.5859	0.8631	0.8571	0.7671	0.7279	0.5899	0.8482	0.7372	0.9811	0.9227	<u>0.9767</u>	0.9218

TABLE VIII
SER VALUES OF ALL THE DETECTORS FOR EACH DATASET.
(THE BEST AND SECOND-BEST SER VALUES ARE HIGHLIGHTED IN BOLD AND UNDERLINED, RESPECTIVELY.)

Datasets	Noise	Methods											
		GRX [8]	LRX [9]	2S-GLRT [13]	RGAE [28]	CRD [16]	RPCA-RX [18]	GTVLRR [21]	LSDM-MoG [22]	Ours (HTV)	Ours (SSTV)	Ours (HSSTV)	Ours (Nuclear)
Pavia Centre	Case 1	0.3100	0.3183	0.2885	0.6335	2.3923	0.2571	0.2917	0.8936	0.2255	0.2593	<u>0.2263</u>	0.2996
	Case 2	0.3571	0.2557	0.2413	0.6821	0.8295	0.3571	0.2819	12.1597	0.2029	0.2851	<u>0.2038</u>	0.3002
	Case 3	5.1301	0.3373	0.3099	1.1698	0.3333	4.7538	2.0711	0.5971	0.2434	0.5183	<u>0.2745</u>	0.5275
	Case 4	2.4600	0.3333	1.4012	1.0136	2.3709	2.3268	1.0691	6.6830	0.1954	0.2445	<u>0.2094</u>	0.3062
	Case 5	5.6498	0.7908	4.7320	1.4581	0.3098	5.6498	2.8912	1.4936	0.2345	0.2782	<u>0.2569</u>	3.4538
Texas Coast	Case 1	0.7941	0.5158	0.4895	0.5627	0.5071	0.6106	2.1871	2.3907	0.4304	0.7328	<u>0.4268</u>	0.4208
	Case 2	8.0902	0.4603	0.4905	0.5642	0.7127	8.1164	1.1296	52.0885	0.3216	0.6725	<u>0.3984</u>	0.9919
	Case 3	9.7969	0.6258	0.6807	2.1172	24.5992	9.7566	13.7380	7.5899	0.5462	1.0194	<u>0.5971</u>	2.1607
	Case 4	5.8262	0.5471	0.5652	0.8885	13.3401	5.7814	9.5081	1.7742	0.3375	0.7358	<u>0.4321</u>	0.9099
	Case 5	17.7300	2.1793	1.4149	3.6671	1.4784	17.7226	23.0340	18.4019	0.4763	0.7678	<u>0.5191</u>	1.9234
Gainesville	Case 1	0.6483	<u>0.4765</u>	0.5193	0.8498	0.7046	0.6525	1.0213	2.1798	0.4366	0.6929	0.8188	0.6814
	Case 2	11.1773	0.3997	0.6253	0.8114	2.4887	11.2864	2.2830	53.1298	0.4064	1.2714	0.6239	1.1372
	Case 3	8.9648	0.5317	<u>0.5336</u>	2.4908	21.5296	8.9382	24.9318	6.9404	0.7225	1.0904	1.0439	1.7269
	Case 4	6.0555	<u>0.5105</u>	2.4938	1.1732	14.3828	6.0518	4.6861	13.8687	0.4247	1.0730	0.6616	0.6893
	Case 5	14.1857	2.0627	3.6538	4.2380	34.0674	14.1857	26.5501	10.4019	0.5942	1.2710	<u>0.8260</u>	3.0953
Los Angeles I	Case 1	2.3508	2.6936	2.6755	2.5445	2.4562	2.3511	2.1591	2.0620	1.9830	<u>2.0172</u>	2.0179	2.0188
	Case 2	2.5652	2.5114	2.3267	2.5349	2.4328	2.5652	1.8937	24.1516	2.1330	2.0595	2.1508	2.0209
	Case 3	6.7355	2.6810	2.7210	2.5916	2.9238	6.4658	3.6725	2.5113	1.9597	2.0574	<u>1.9796</u>	2.0154
	Case 4	4.2621	2.5159	2.4091	2.5075	9.9344	4.1680	2.4878	4.0462	<u>2.0186</u>	2.0601	<u>2.0682</u>	2.0110
	Case 5	6.1737	2.6371	5.0135	2.7878	21.2684	6.1737	4.0323	2.4816	<u>2.2474</u>	2.2913	2.2509	2.1144
Los Angeles II	Case 1	1.9880	2.1461	2.0689	1.8216	2.0213	1.9880	2.4024	2.6732	1.2274	1.4299	<u>1.2739</u>	2.2254
	Case 2	8.3143	2.0325	1.7170	1.8242	22.1677	8.2991	2.1595	50.0047	1.2568	1.4050	<u>1.2993</u>	4.6942
	Case 3	10.9514	2.2229	2.3067	2.7506	5.2911	10.8474	23.2898	6.0441	1.2929	1.5730	<u>1.2989</u>	1.9827
	Case 4	7.6810	2.2115	2.6275	2.0107	4.9489	7.6848	12.0634	17.2633	<u>1.2693</u>	1.3380	1.2659	1.8901
	Case 5	12.6619	2.1845	2.5621	4.5622	2.3600	12.6619	21.6624	5.9420	1.3355	1.5760	<u>1.3770</u>	2.1841
San Diego	Case 1	1.4744	1.3251	1.3599	<u>0.9946</u>	1.1032	1.4868	1.1354	5.1526	1.0127	1.2677	1.0214	0.9883
	Case 2	2.7096	1.0241	1.1699	<u>0.9925</u>	1.4712	2.7666	1.2227	10.0407	0.9473	1.0379	1.0052	1.0372
	Case 3	7.1685	1.3027	1.3925	2.8969	1.7426	7.2265	10.1626	13.0415	1.0407	1.4917	<u>1.0741</u>	1.1514
	Case 4	5.2110	1.3172	1.3705	1.3933	2.8876	5.2731	2.3920	12.9348	0.9604	1.0135	<u>0.9869</u>	1.0509
	Case 5	10.2425	3.2969	3.0792	5.1791	1.9135	10.2301	6.0407	18.1592	0.9766	1.1832	<u>1.0246</u>	1.4488

other hand, GTVLRR and the proposed method detected only anomalies. Among them, the proposed method using HTV or

HSSTV succeeded in generating a clear detection map.

Fig. 3 (a) depicts the ROC curves of all the detectors for

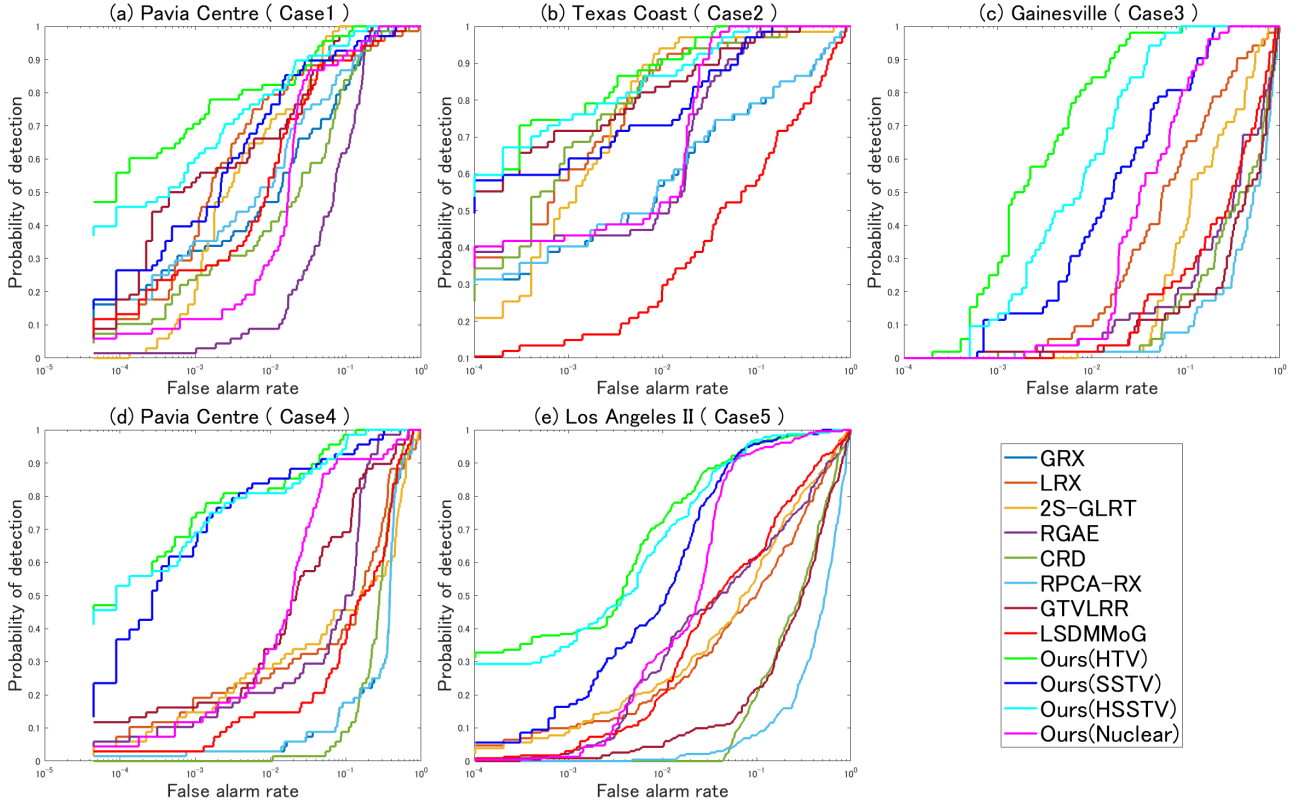


Fig. 3. ROC curves of all the detectors for each dataset.

Pavia Centre. The proposed method using HTV, SSTV, or HSSTV has an overall higher probability of detection than the other methods, which is consistent with the visual results.

2) *Case 2 (Gaussian noise)*: Tables VII and VIII show that GRX, RPCA-RX, and LSDM-MoG have worse AUC and SER values than those of the results in Case 1 for all datasets. In contrast, the other methods (including, interestingly, those designed without explicit consideration of noise) have little change in their values. LRX, 2S-GLRT, and CRD use the surrounding pixels of the test pixel as a dictionary, and RGAE and GTVLRR include graph regularization in their objective functions. Therefore, methods designed to handle such spatial information may be robust to Gaussian noise. On the other hand, the proposed method achieved overall superior AUC and SER values because the second constraint in Prob. (8) allows estimating the anomaly and background parts simultaneously while eliminating Gaussian noise. In particular, the proposed method using HTV, SSTV, or HSSTV performs better than the proposed method using the nuclear norm.

Fig. 5 and 3 (b) show the detection maps and ROC curves for Texas Coast generated by all the detectors, respectively. The detection maps generated by GRX, RPCA-RX, and LSDM-MoG are noisy and the probability of detection for these methods is low. In contrast, anomalies can be clearly identified from the detection maps generated by other methods. Among them, the proposed method using HTV detected the anomalies while suppressing the most background.

3) *Case 3 (Non-Gaussian noise)*: From Tables VII and VIII, it can be seen that all the existing methods fail

to detect anomalies. This is because these methods are designed without considering the effect of non-Gaussian noise, which makes it difficult to distinguish between background, anomalies, and such noise. On the other hand, the proposed method achieved almost the same level of performance. This is due to the superior modeling of stripe noise by the third term and the first constraint in Prob. (8), and sparse noise by the third constraint. Comparing the background regularization, the proposed method using HTV or HSSTV performs better.

Fig. 6 and 3 (c) show the detection maps and ROC curves for Gainesville generated by all the detectors, respectively. GRX, RGAE, CRD, RPCA-RX, GTVLRR, and LSDM-MoG are clearly affected by non-Gaussian noise, in particular, stripe noise is noticeable in the detection map of LSDM-MoG. On the other hand, the detection maps of LRX and 2S-GLRT are noise-free, but these methods do not detect any anomalies at all, as indicated by the ROC curves and AUC values. Note that the SER values of these methods are superior, but this is because most of the pixels are detected as background pixels. The detection maps of the proposed method contain no noise and detect all anomalies, especially the proposed method using HTV has excellent background suppression capability.

4) *Case 4 & 5 (Mixed noise)*: Fig. 7 and 8 show the detection maps for Pavia Centre in Case 4 and Los Angeles I in Case 5, respectively, generated by all the detectors. Fig. 3 (d) and (e) also depict the ROC curves for Pavia Centre in Case 4 and Los Angeles I in Case 5, respectively. These figures and Tables VII and VIII illustrate that the detection performance of all the existing methods is significantly degraded compared

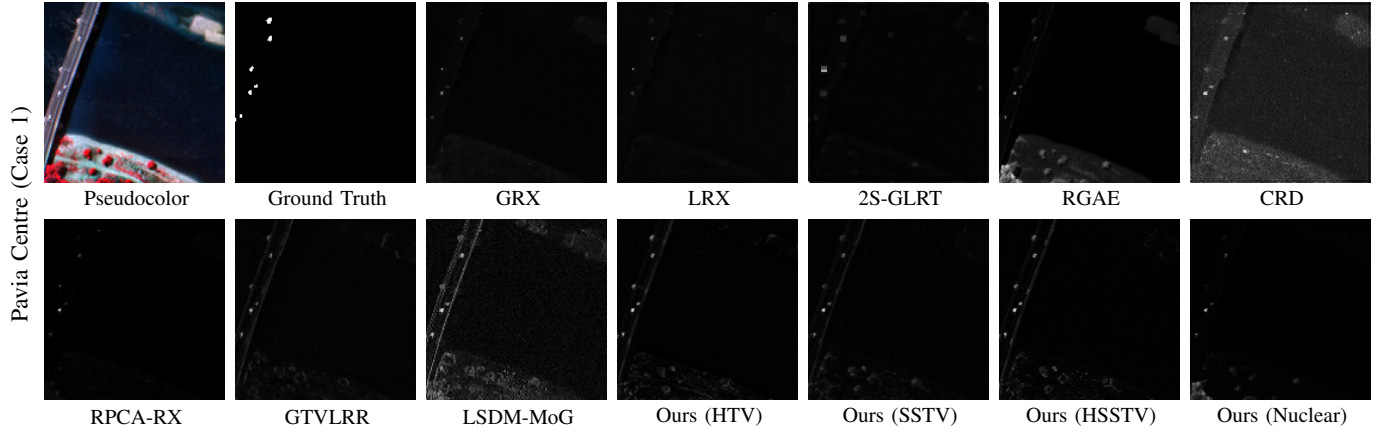


Fig. 4. Resulting detection maps for Pavia Centre in Case 1 generated by all the detectors.

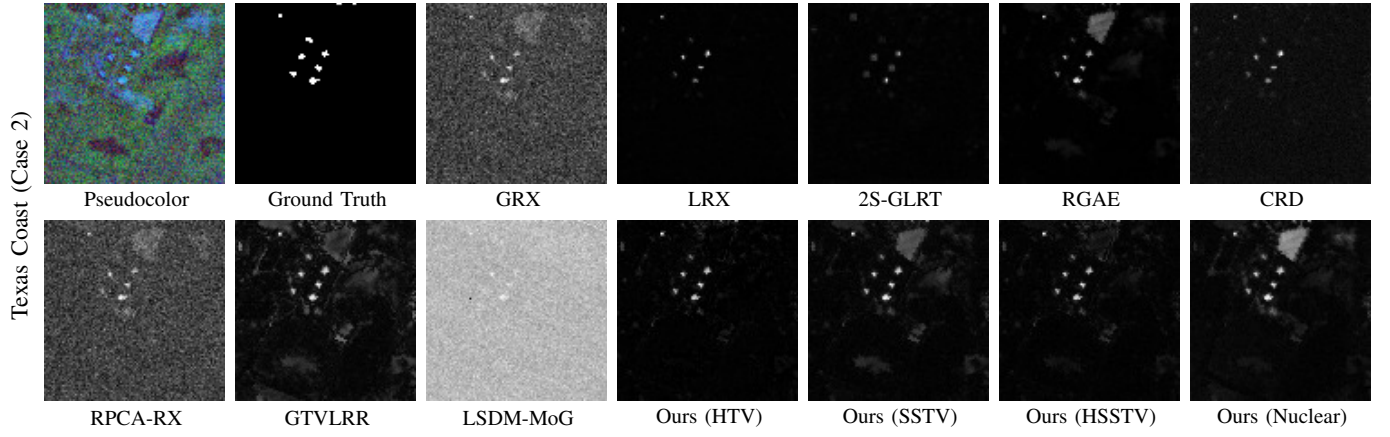


Fig. 5. Resulting detection maps for Texas Coast in Case 2 generated by all the detectors.

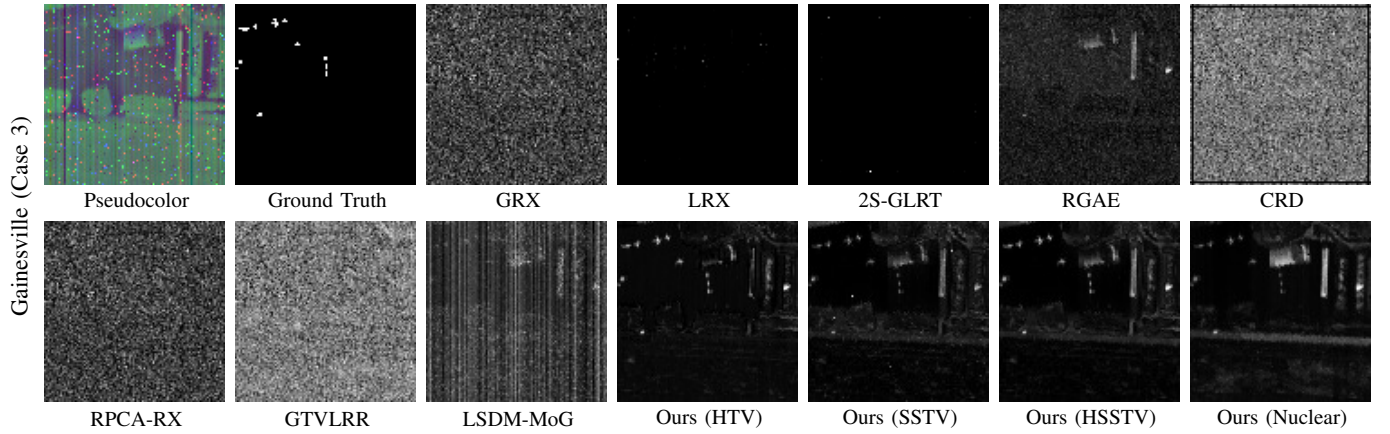


Fig. 6. Resulting detection maps for Gainesville in Case 3 generated by all the detectors.

to the results of Case 1. This is because, as mentioned in the discussion of Case 3, these methods are designed for the case where the HS image is noise-free or only contaminated with Gaussian noise and cannot accurately separate background, anomalies, and mixed noise. In contrast, the proposed method can handle all three types of noise, resulting in detection performance equivalent to that of Case 1.

E. Parameter Analysis

In the proposed method, the four parameters, λ_1 , λ_2 , ε , and α , affect the detection performance. Therefore, we describe the parameter analysis of the proposed method using HTV, which achieved the best detection performance among the specific designs of background characterization functions.

To investigate the influence of λ_1 , we set $\varepsilon = \alpha = \lambda_2 = 0$ and conducted experiments using data from Case 1. Fig. 9 shows the AUC values with different λ_1 in each dataset. In the data except for Los Angeles I, the AUC curve shows a

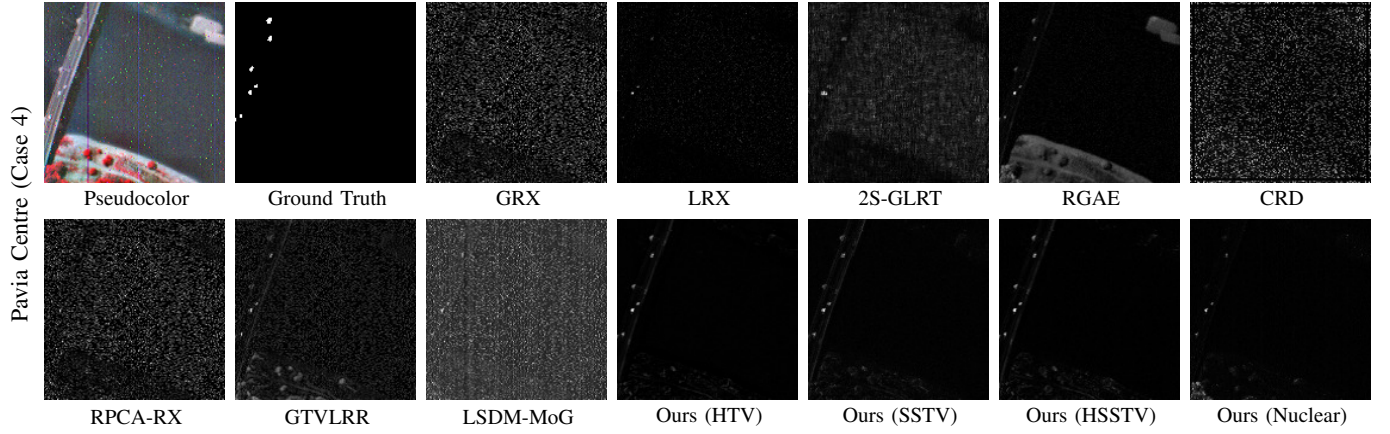


Fig. 7. Resulting detection maps for Pavia Centre in Case 4 generated by all the detectors.

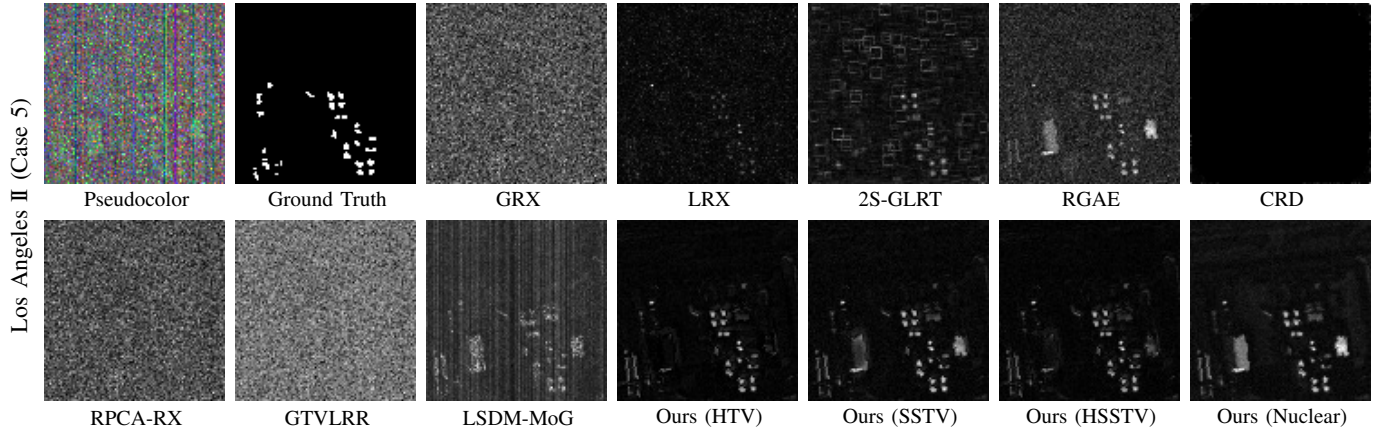


Fig. 8. Resulting detection maps for Los Angeles II in Case 5 generated by all the detectors.

downward trend after reaching a peak at λ_1 of 0.75 or 1. In Los Angeles I, on the other hand, the AUC values are almost the same when λ_1 is between 0.01 and 0.5, and then the AUC curve shows a downward trend. Based on these results, we recommend setting λ_1 to 0.5, 0.75, or 1.

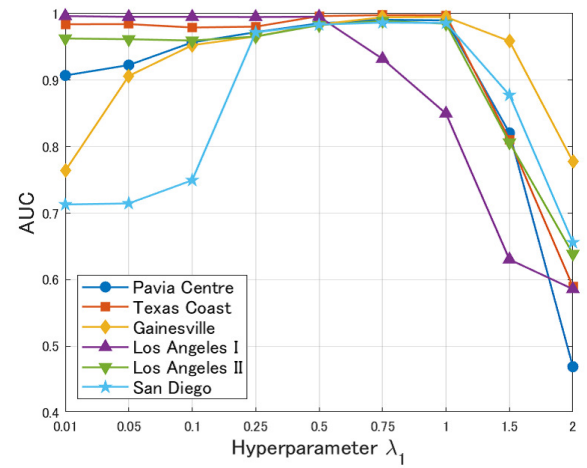
To investigate the influence of λ_2 and η , i.e., ε and α (see Eq. (27)), we fixed λ_1 to 0.5, 0.75, or 1 and conducted experiments using data from Case 5. Fig. 10 shows the AUC values for different λ_2 and η for Pavia Centre in Case 5. Almost the same AUC values are obtained by changing λ_2 , reaching a peak at either 0.025, 0.05, or 0.075. Experiments with other data showed a similar trend, so we recommend setting λ_2 to one of these values.

In most cases, the AUC value is maximum when η is set to 0.9 or 0.95. In the experiments in this article, the highest AUC values were often observed when η was 0.9, so we recommend setting η to 0.9.

F. Summary

We summarize the experimental discussion as follows:

- The experimental results in Case 1 show that the proposed method achieves state-of-the-art detection performance. This is due to the proper modeling of the background and anomaly parts.
- The experimental results in Cases 2, 3, 4, and 5 show that the proposed method is robust to various types of

Fig. 9. Parameter analysis of λ_1 for all datasets in Case 1.

noise. The reason for this is that the modeling of each noise is adequate, allowing for the estimation of the two parts simultaneously with noise removal.

- Among the background characterizations, the proposed method using HTV achieved the best detection performance. This is because it is most reasonable to characterize the spatial piecewise smoothness of the background

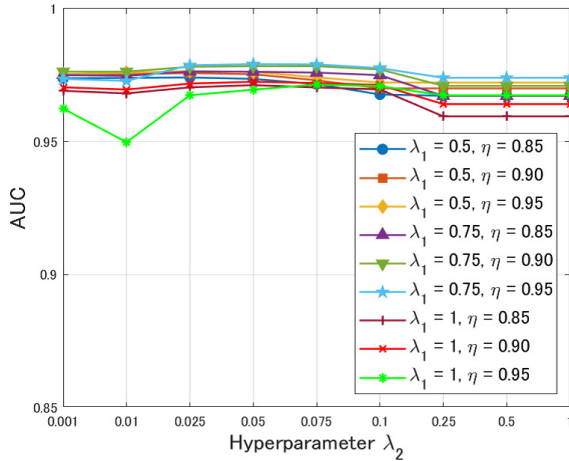


Fig. 10. Parameter analysis of λ_2 and η for Pavia Centre in Case 5.

part.

V. CONCLUSION

In this article, we have proposed a noise-robust HS anomaly detection method. To explicitly handle mixed noise, we have modeled three types of noise. We have formulated a constrained convex optimization problem for the simultaneous estimation of background and anomaly parts and these noise from an HS image and then developed an optimization algorithm based on P-PDS. Experimental results on six HS datasets demonstrate that the proposed method achieves detection performance comparable to state-of-the-art methods in noise-free cases and is robust to various types of noise in noisy cases.

REFERENCES

- [1] P. Ghamisi, N. Yokoya, J. Li, W. Liao, S. Liu, J. Plaza, B. Rasti, and A. Plaza, "Advances in hyperspectral image and signal processing: A comprehensive overview of the state of the art," *IEEE Geosci. Remote Sens. Mag.*, vol. 5, no. 4, pp. 37–78, Dec. 2017.
- [2] J. M. Bioucas-Dias, A. Plaza, N. Dobigeon, M. Parente, Q. Du, P. Gader, and J. Chanussot, "Hyperspectral unmixing overview: Geometrical, statistical, and sparse regression-based approaches," *IEEE J. Sel. Topics Appl. Earth Observ. Remote Sens.*, vol. 5, no. 2, pp. 354–379, Apr. 2012.
- [3] D. W. J. Stein, S. G. Beaven, L. E. Hoff, E. M. Winter, A. P. Schaum, and A. D. Stocker, "Anomaly detection from hyperspectral imagery," *IEEE Signal Process. Mag.*, vol. 19, no. 1, pp. 58–69, Jan. 2002.
- [4] H. Su, Z. Wu, H. Zhang, and Q. Du, "Hyperspectral anomaly detection: A survey," *IEEE Geosci. Remote Sens. Mag.*, vol. 10, no. 1, pp. 64–90, Mar. 2022.
- [5] Y. Xu, L. Zhang, B. Du, and L. Zhang, "Hyperspectral anomaly detection based on machine learning: An overview," *IEEE J. Sel. Topics Appl. Earth Observ. Remote Sens.*, vol. 15, pp. 3351–3364, 2022.
- [6] S. Matteoli, M. Diani, and G. Corsini, "A tutorial overview of anomaly detection in hyperspectral images," *IEEE Aerosp. Electron. Syst. Mag.*, vol. 25, no. 7, pp. 5–28, Jul. 2010.
- [7] S. Matteoli, M. Diani, and J. Theiler, "An overview of background modeling for detection of targets and anomalies in hyperspectral remotely sensed imagery," *IEEE J. Sel. Topics Appl. Earth Observ. Remote Sens.*, vol. 7, no. 6, pp. 2317–2336, Jun. 2014.
- [8] I. S. Reed and X. Yu, "Adaptive multiple-band CFAR detection of an optical pattern with unknown spectral distribution," *IEEE Trans. Acoust., Speech, Signal Process.*, vol. 38, no. 10, pp. 1760–1770, Oct. 1990.
- [9] J. M. Molero, E. M. Garzon, I. Garcia, and A. Plaza, "Analysis and optimizations of global and local versions of the RX algorithm for anomaly detection in hyperspectral data," *IEEE J. Sel. Topics Appl. Earth Observ. Remote Sens.*, vol. 6, no. 2, pp. 801–814, Apr. 2013.
- [10] W.-M. Liu and C.-I. Chang, "Multiple-window anomaly detection for hyperspectral imagery," *IEEE J. Sel. Topics Appl. Earth Observ. Remote Sens.*, vol. 6, no. 2, pp. 644–658, Apr. 2013.
- [11] H. Kwon and N. M. Nasrabadi, "Kernel RX-algorithm: A nonlinear anomaly detector for hyperspectral imagery," *IEEE Trans. Geosci. Remote Sens.*, vol. 43, no. 2, pp. 388–397, Feb. 2005.
- [12] Q. Guo, B. Zhang, Q. Ran, L. Gao, J. Li, and A. Plaza, "Weighted-RXD and linear filter-based RXD: Improving background statistics estimation for anomaly detection in hyperspectral imagery," *IEEE J. Sel. Topics Appl. Earth Observ. Remote Sens.*, vol. 7, no. 6, pp. 2351–2366, Jun. 2014.
- [13] J. Liu, Z. Hou, W. Li, R. Tao, D. Orlando, and H. Li, "Multipixel anomaly detection with unknown patterns for hyperspectral imagery," *IEEE Trans. Neural Netw. Learn. Syst.*, vol. 33, no. 10, pp. 5557–5567, Oct. 2022.
- [14] J. Li, H. Zhang, L. Zhang, and L. Ma, "Hyperspectral anomaly detection by the use of background joint sparse representation," *IEEE J. Sel. Topics Appl. Earth Observ. Remote Sens.*, vol. 8, no. 6, pp. 2523–2533, Jun. 2015.
- [15] Q. Ling, Y. Guo, Z. Lin, and W. An, "A constrained sparse representation model for hyperspectral anomaly detection," *IEEE Trans. Geosci. Remote Sens.*, vol. 57, no. 4, pp. 2358–2371, Apr. 2019.
- [16] W. Li and Q. Du, "Collaborative representation for hyperspectral anomaly detection," *IEEE Trans. Geosci. Remote Sens.*, vol. 53, no. 3, pp. 1463–1474, Mar. 2015.
- [17] H. Su, Z. Wu, Q. Du, and P. Du, "Hyperspectral anomaly detection using collaborative representation with outlier removal," *IEEE J. Sel. Topics Appl. Earth Observ. Remote Sens.*, vol. 11, no. 12, pp. 5029–5038, Dec. 2018.
- [18] G. Liu, Z. Lin, S. Yan, J. Sun, Y. Yu, and Y. Ma, "Robust recovery of subspace structures by low-rank representation," *IEEE Trans. Pattern Anal. Mach. Intell.*, vol. 35, no. 1, pp. 171–184, Jan. 2013.
- [19] Y. Xu, Z. Wu, J. Li, A. Plaza, and Z. Wei, "Anomaly detection in hyperspectral images based on low-rank and sparse representation," *IEEE Trans. Geosci. Remote Sens.*, vol. 54, no. 4, pp. 1990–2000, Apr. 2016.
- [20] Y. Zhang, B. Du, L. Zhang, and S. Wang, "A low-rank and sparse matrix decomposition-based mahalanobis distance method for hyperspectral anomaly detection," *IEEE Trans. Geosci. Remote Sens.*, vol. 54, no. 3, pp. 1376–1389, Oct. 2016.
- [21] T. Cheng and B. Wang, "Graph and total variation regularized low-rank representation for hyperspectral anomaly detection," *IEEE Trans. Geosci. Remote Sens.*, vol. 58, no. 1, pp. 391–406, Jan. 2020.
- [22] L. Li, W. Li, Q. Du, and R. Tao, "Low-rank and sparse decomposition with mixture of gaussian for hyperspectral anomaly detection," *IEEE Trans. Cybern.*, vol. 51, no. 9, pp. 4363–4372, Sep. 2021.
- [23] L. Li, W. Li, Y. Qu, C. Zhao, R. Tao, and Q. Du, "Prior-based tensor approximation for anomaly detection in hyperspectral imagery," *IEEE Trans. Neural Netw. Learn. Syst.*, vol. 33, no. 3, pp. 1037–1050, Mar. 2022.
- [24] M. Wang, Q. Wang, D. Hong, S. K. Roy, and J. Chanussot, "Learning tensor low-rank representation for hyperspectral anomaly detection," *IEEE Trans. Cybern.*, vol. 53, no. 1, pp. 679–691, Jan. 2023.
- [25] E. Bati, A. Çalışkan, A. Koz, and A. A. Alatan, "Hyperspectral anomaly detection method based on auto-encoder," in *Proc. Image Signal Process. Remote Sens.*, vol. 9643, Oct. 2015, pp. 220–226.
- [26] S. Chang, B. Du, and L. Zhang, "A sparse autoencoder based hyperspectral anomaly detection algorithm using residual of reconstruction error," in *Proc. IEEE Int. Geosci. Remote Sens. Symp. (IGARSS)*, Jul. 2019, pp. 5488–5491.
- [27] X. Lu, W. Zhang, and J. Huang, "Exploiting embedding manifold of autoencoders for hyperspectral anomaly detection," *IEEE Trans. Geosci. Remote Sens.*, vol. 58, no. 3, pp. 1527–1537, Mar. 2020.
- [28] G. Fan, Y. Ma, X. Mei, F. Fan, J. Huang, and J. Ma, "Hyperspectral anomaly detection with robust graph autoencoders," *IEEE Trans. Geosci. Remote Sens.*, vol. 60, pp. 1–14, Jul. 2022.
- [29] B. Rasti, P. Scheunders, P. Ghamisi, G. Licciardi, and J. Chanussot, "Noise reduction in hyperspectral imagery: Overview and application," *Remote Sens.*, vol. 10, no. 3, p. 482, Mar. 2018.
- [30] M. V. Afonso, J. M. Bioucas-Dias, and M. A. Figueiredo, "An augmented Lagrangian approach to the constrained optimization formulation of imaging inverse problems," *IEEE Trans. Image Process.*, vol. 20, no. 3, pp. 681–695, Mar. 2011.
- [31] G. Chierchia, N. Pustelnik, J.-C. Pesquet, and B. Pesquet-Popescu, "Epigraphical projection and proximal tools for solving constrained convex optimization problems," *Signal, Image Video Process.*, vol. 9, no. 8, pp. 1737–1749, 2015.

- [32] S. Ono and I. Yamada, "Signal recovery with certain involved convex data-fidelity constraints," *IEEE Trans. Signal Process.*, vol. 63, no. 22, pp. 6149–6163, Nov. 2015.
- [33] S. Ono, "Primal-dual plug-and-play image restoration," *IEEE Signal Process. Lett.*, vol. 24, no. 8, pp. 1108–1112, Aug. 2017.
- [34] S. Ono, " L_0 gradient projection," *IEEE Trans. Image Process.*, vol. 26, no. 4, pp. 1554–1564, Apr. 2017.
- [35] T. Pock and A. Chambolle, "Diagonal preconditioning for first order primal-dual algorithms in convex optimization," in *Proc. Int. Conf. Comput. Vis. (ICCV)*, Nov. 2011, pp. 1762–1769.
- [36] K. Naganuma and S. Ono, "Operator-norm-based variable-wise diagonal preconditioning for automatic stepsize selection of a primal-dual splitting algorithm," in *Proc. Eur. Signal Process. Conf. (EUSIPCO)*, Aug. 2022, pp. 2041–2045.
- [37] K. Naganuma and S. Ono, "Variable-wise diagonal preconditioning for primal-dual splitting: Design and applications," *IEEE Trans. Signal Process.*, vol. 71, pp. 3281–3295, 2023.
- [38] K. Sato and S. Ono, "Robust hyperspectral anomaly detection with simultaneous mixed noise removal via constrained convex optimization," in *Proc. IEEE Int. Conf. Acoust., Speech, Signal Process. (ICASSP)*, IEEE, 2023, pp. 1–5.
- [39] H. H. Bauschke and P. L. Combettes, *Convex Analysis and Monotone Operator Theory in Hilbert Spaces*. Springer, 2011.
- [40] A. Beck, *First-order methods in optimization*. SIAM, 2017.
- [41] A. Chambolle and T. Pock, "A first-order primal-dual algorithm for convex problems with applications to imaging," *J. Math. Imaging Vision*, vol. 40, no. 1, pp. 120–145, 2011.
- [42] K. Naganuma and S. Ono, "A general destriping framework for remote sensing images using flatness constraint," *IEEE Trans. Geosci. Remote Sens.*, vol. 60, pp. 1–16, 2022.
- [43] L. Condat, "Fast projection onto the simplex and the l_1 ball," *Math. Program.*, vol. 158, no. 1, pp. 575–585, Jul. 2016.
- [44] Q. Yuan, L. Zhang, and H. Shen, "Hyperspectral image denoising employing a spectral-spatial adaptive total variation model," *IEEE Trans. Geosci. Remote Sens.*, vol. 50, no. 10, pp. 3660–3677, Oct. 2012.
- [45] H. K. Aggarwal and A. Majumdar, "Hyperspectral image denoising using spatio-spectral total variation," *IEEE Geosci. Remote Sens. Lett.*, vol. 13, no. 3, pp. 442–446, Feb. 2016.
- [46] S. Takeyama, S. Ono, and I. Kumazawa, "A constrained convex optimization approach to hyperspectral image restoration with hybrid spatio-spectral regularization," *Remote Sens.*, vol. 12, no. 21, p. 3541, Jan. 2020.
- [47] A. Chambolle, "An algorithm for total variation minimization and applications," *J. Math. Imag. Vis.*, vol. 20, pp. 89–97, 2004.
- [48] X. Kang, X. Zhang, S. Li, K. Li, J. Li, and J. A. Benediktsson, "Hyperspectral anomaly detection with attribute and edge-preserving filters," *IEEE Trans. Geosci. Remote Sens.*, vol. 55, no. 10, pp. 5600–5611, Oct. 2017.
- [49] J. Kerekes, "Receiver operating characteristic curve confidence intervals and regions," *IEEE Geosci. Remote Sens. Lett.*, vol. 5, no. 2, pp. 251–255, Apr. 2008.
- [50] M. Díaz, R. Guerra, S. López, and R. Sarmiento, "An algorithm for an accurate detection of anomalies in hyperspectral images with a low computational complexity," *IEEE Trans. Geosci. Remote Sens.*, vol. 56, no. 2, pp. 1159–1176, Feb. 2018.

PLACE
PHOTO
HERE

Shunsuke Ono (S'11–M'15–SM'23) received a B.E. degree in Computer Science in 2010 and M.E. and Ph.D. degrees in Communications and Computer Engineering in 2012 and 2014 from the Tokyo Institute of Technology, respectively.

From April 2012 to September 2014, he was a Research Fellow (DC1) of the Japan Society for the Promotion of Science (JSPS). He is currently an Associate Professor in the Department of Computer Science, School of Computing, Tokyo Institute of Technology. From October 2016 to March 2020

and from October 2021 to present, he was/is a Researcher of Precursory Research for Embryonic Science and Technology (PRESTO), Japan Science and Technology Agency (JST), Tokyo, Japan. His research interests include signal processing, image analysis, remote sensing, mathematical optimization, and data science.

Dr. Ono received the Young Researchers' Award and the Excellent Paper Award from the IEICE in 2013 and 2014, respectively, the Outstanding Student Journal Paper Award and the Young Author Best Paper Award from the IEEE SPS Japan Chapter in 2014 and 2020, respectively, the Funai Research Award from the Funai Foundation in 2017, the Ando Incentive Prize from the Foundation of Ando Laboratory in 2021, and the Young Scientists' Award from MEXT in 2022. He has been an Associate Editor of IEEE TRANSACTIONS ON SIGNAL AND INFORMATION PROCESSING OVER NETWORKS since 2019.

PLACE
PHOTO
HERE

Koyo Sato (S'23) received a B.E. degree in Computer Science in 2022 from the Tokyo Institute of Technology.

He is currently pursuing an M.E. degree at the Department of Computer Science in the Tokyo Institute of Technology.